

RESEARCH ARTICLE

A computational model of cell viability and proliferation of extrusion-based 3D-bioprinted constructs during tissue maturation process

Patrizia Gironi¹, Ludovico Petraro¹, Silvia Santoni^{1,2}, Luca Dedé³,
Bianca Maria Colosimo^{1*}

¹Department of Mechanical Engineering, Politecnico di Milano, Via Privata Giuseppe La Masa, 1, Milano 20156, Italy

²Department of Chemistry, Materials and Chemical Engineering “Giulio Natta”, Politecnico di Milano, Piazza Leonardo da Vinci, 32, 20133, Milan, Italy

³MOX - Modeling and Scientific Computing, Dipartimento di Matematica, Politecnico di Milano, Piazza Leonardo da Vinci 32, Milano 20133, Italy

Abstract

3D bioprinting is a novel promising solution for living tissue fabrication, with several potential advantages in many different applicative sectors. However, the implementation of complex vascular networks remains as one of the limiting factors for the production of complex tissues and for bioprinting scale-up. In this work, a physics-based computational model is presented to describe nutrients diffusion and consumption phenomena in bioprinted constructs. The model—a system of partial differential equations that is approximated by means of the finite element method—allows for the description of cell viability and proliferation, and it can be easily adapted to different cell types, densities, biomaterials, and 3D-printed geometries, thus allowing a preassessment of cell viability within the bioprinted construct. The experimental validation is performed on bioprinted specimens to assess the ability of the model to predict changes in cell viability. The proposed model constitutes a proof of concept of digital twinning of biofabricated constructs that can be suitably included in the basic toolkit for tissue bioprinting.

Keywords: Bioprinting; Oxygen; Glucose; Mathematical model; Finite element method; Validation

***Corresponding author:**

Bianca Maria Colosimo
(biancamaria.colosimo@polimi.it)

Citation: Gironi P, Petraro L, Santoni S, *et al.*, 2023, A computational model of cell viability and proliferation of extrusion-based 3D-bioprinted constructs during tissue maturation process.

Int J Bioprint, 9(4): 741.
<https://doi.org/10.18063/ijb.741>

Received: January 19, 2023

Accepted: March 08, 2023

Published Online: April 28, 2023

Copyright: © 2023 Author(s).

This is an Open Access article distributed under the terms of the Creative Commons Attribution License, permitting distribution, and reproduction in any medium, provided the original work is properly cited.

Publisher's Note: Whioce Publishing remains neutral with regard to jurisdictional claims in published maps and institutional affiliations.

1. Introduction

Over the last decades, tissue engineering has been widely exploited for the regeneration of damaged tissues and organs, especially to compensate for the mismatch between organ demand and availability^[1]. However, the spatial control and density obtained through cell seeding onto premade scaffolds are not suitable for the regeneration of complex tissues. In this context, 3D bioprinting constitutes a promising solution for complex biological tissues with high cell density and different cell types^[2]. The interest toward 3D bioprinting has increased exponentially in the last two decades both in academic institutions and in the market field, as thoroughly reported by

Santoni *et al.*^[3]. Significant effort is being put into the optimization of the 3D printing process and into the material functionalization.

Bioprinting generically refers to different additive manufacturing (AM) techniques applied to the biological field. Bioprinting techniques are classified according to the technique of layer-wise deposition, similarly to the polymer AM standards (ISO/ASTM 52900)^[4,5]. Extrusion-based bioprinting is very common due to its flexibility and ease of use. It involves the deposition of a bioink that is a biocompatible hydrogel embedded with cells, in a layer-by-layer fashion. A dispensing unit extrudes the bioink from the cartridge through the application of a pneumatic mechanical force, that can be piston-driven or screw-driven, or a solenoid-based force^[6]. The presence of multiple printheads enables the extrusion of different materials and cell types in a single print. A major drawback of this technique is the poor resolution of the printed samples and the impossibility to print features at the micro scale. This technique is known to retain a high percentage of cell viability, which is mainly affected by shear stresses. Another technique for dispensing a hydrogel is inkjet-based bioprinting. This method allows for the dispensing of picoliter and nanoliter drops through a piezoelectric or thermic actuator. Droplet impact velocity and droplet volume have been identified as the main factors affecting cell viability^[7]. Another bioprinting technique is vat polymerization. This method consists of the photopolymerization of a photoink, i.e., a photoresponsive material embedded with cells. A light source is projected to the points intended to be polymerized and the construct is built layer-by-layer^[8]. This technique allows for the fabrication of high-resolution features but requires that the materials are photopolymerizable and cannot be used with different materials at the same time. Digital light processing and two-photon polymerization exploit the same concept and enable higher printing speed and resolution. A crucial point of vat photopolymerization is the effect on cell viability of some photoinitiators and laser sources, which must be chosen accurately.

Current applications of 3D bioprinting are focused on the realization of pathological models, organ-on-chips, and microfluidic systems, which better replicate the *in vivo* environment. The ultimate goal is the production of tissues and organs starting from the patients' own cells. Different organs have been addressed, ranging from simple ones like skin and cartilage to more complex and articulated structures, such as the heart^[9]. One of the main unsolved issues in bioprinting is the capability to develop constructs with embedded vascularization. Large tissues with high cell density are prone to a lack of nutrients, especially in the areas far

from the boundaries. This possibly leads to cell suffering and limited growth, with eventual cell death in the long term^[10,11]. The implementation of vascular networks within the bioprinted constructs is needed to allow for a more uniform distribution of nutrients to all cells; therefore, it constitutes an important step toward the use of bioprinting for clinical applications.

Two main phenomena that drive cell viability and maturation in 3D-bioprinted constructs are nutrient diffusion and consumption, as well as cell proliferation as a function of their spatial location in the 3D geometry. With respect to the nutrient diffusion and consumption, the Fick's law is usually considered the reference to represent these phenomena, which can be modeled as the mass transport of a solute in a solution using diffusion partial differential equations (PDEs). An interesting example of a Fick's law model to represent nutrients diffusion was presented by McMurtrey in 2016^[10], who developed a mathematical model of diffusion and metabolism in basic 3D constructs applied to cerebral organoids. The consumption rates of different cell types and the concentration and diffusion coefficients of oxygen and glucose in basic biological environments were investigated. However, the models were applied to simple geometries, such as one-dimensional (1D), planar, cylindric, or spherical structures, and can be solved analytically. Therefore, one of the main limitations of McMurtrey's approach is the 1D and quasi-stationary representation of the problem and the limiting assumption on nutrient consumption, being either neglected or considered constant. Other works in the literature provided more complex descriptions of the oxygen consumption rate. The most common one is the Michaelis–Menten's law, which considers the actual consumption as the maximum consumption times the ratio between the current concentration and the current concentration summed to the Michaelis–Menten constant. The latter is defined as the concentration at which 50% of the maximum consumption occurs. Ehsan and George^[12] applied and validated Michaelis–Menten's law with reference to human lung fibroblasts. Similarly, Magliaro *et al.*^[13] showed that oxygen consumption rates are well described by Michaelis–Menten kinetics given that reaction parameters are not literature constants but depend on cell density. The authors of the latter investigated the consumption phenomenon in detail, which was found to be dependent on oxygen concentration, cell concentration, and variation of the parameters. They also compared consumption in 2D and 3D environments and developed a model for the diffusion and consumption of oxygen in 3D constructs. The cooperative behavior of cells, which can adapt their oxygen consumption according to cell concentration, represents one of the key novelty factors of this study. In both cited

works, a set of limiting assumptions were again considered, namely the 1D simplification and the neglect of cellular proliferation.

With regards to cell proliferation and death, many models have been developed and exploited to explain various cell growth curves under different conditions. Jin and Lei^[14] developed a mathematical model based on the logistic growth model to study the role of autophagy in yeast cell population dynamics in response to starvation. The logistic model is a basic paradigm in population ecology, first established by Verhulst in 1838^[15]. The logistic model is a reasonable approximation of growth behavior in many situations and is qualitatively correct, as it captures the phenomenon of exponential growth at low population levels and saturation in the case of high population levels^[14]. Several works are found in the literature about mathematical modeling of nutrient diffusion and cell proliferation and death^[16-19]. They take place within the context of avascular tumor models and cell spheroids, where cells occupy the entire volume of the spheroid. Cell proliferation and death is modeled through a change in the spheroid size, which is not applicable to 3D-printed constructs where cells are embedded in a hydrogel. In 2009, Higuera *et al.*^[20] proposed a mathematical model to assess the proliferation of human mesenchymal stem cells (hMSCs) in 2D culture over glucose and glutamine. Oxygen, on the other hand, was neglected in the model since it was deemed to be sufficient for cell proliferation. The growth phenomenon was modeled using the Monod equation, an empirical model very similar to the Michaelis-Menten law in its formulation, where the consumption rate is replaced by the growth rate. In the model, the possible cell death was considered through a constant death rate in the mass balance. Yet, because of the short time of culture considered, it was then neglected. Besides, the model would predict a forever lasting growth, because no terms to stop cellular proliferation are considered. In 2019, Xu *et al.*^[21] proposed an analytical solution for a hybrid Logistic-Monod equation. In this work, the authors developed a realistic PDE model based on diffusion and consumption of nutrients and cell growth and applied it to 3D-printed constructs. Yet, the model did not consider the three-dimensionality of the phenomena and the model was solved analytically.

The aim of our work is to develop a versatile computational model combining the diffusion and consumption of nutrients and the consequent cell proliferation and death in 3D-bioprinted construct. The differential model, a system of PDEs approximated by means of the finite element method, enhances the understanding of how these phenomena influence cell distribution in the construct and the consequent success of

the generated tissue. It also acts as a powerful tool for the design of tissues embedded with proper vascular networks to guarantee viability for all cells and proper tissue formation. To the best of our knowledge, no other work on PDE-based models and finite element simulation of these phenomena present in the literature is specifically applied to bioprinting. In the present work, some important details in the model with respect to the already proposed ones were added. First, the dynamic state of the 3D-bioprinted constructs was modeled, considering both temporal and spatial variations. Besides, glucose and oxygen diffusion were analyzed at the same time to study their effect on cellular proliferation. The influence of the substance concentration on the consumption rate was considered, and cell proliferation and death were introduced. To consider the competitive and cooperative behaviors of cells in the different phases of proliferation, we combined the typical Monod expression with the Lotka-Volterra model of population growth. This combination accounts for the transition from the substrate-limiting phase, in which the limiting growth factor is the substance shortage, to the self-limiting phase, in which cells decrease their proliferation rate. To account for both substrate-limiting and self-inhibiting factors and to describe the transition between the two phases, the Monod equation was simply multiplied with the self-inhibiting factor.

All the input parameters required by the model were derived from the existing literature. A second step of model validation was carried out with an experiment measuring cell viability observed over time on extrusion-based 3D-bioprinted samples. This validation step allowed a clear understanding of the most relevant parameters affecting the prediction capability of the simulation model. In fact, by comparing the cell viability predicted by the model with the one empirically assessed, the first step of model calibration was performed by tuning all the model parameters in order to minimize the discrepancy between the predicted and the real cell viability observed over time. A further sensitivity analysis on input parameters allowed us to identify the most crucial parameters influencing the prediction capability of the simulation model, namely the growth rate and the maximum cell density. Given the high number of input parameters and the difficulty in measuring them, which results in a broad range of values available in the literature, this sensitivity analysis represents a relevant byproduct of this work, as it allows the interested reader to clearly identify critical parameters that need to be accurately estimated.

Eventually, the last part of this work is meant to show how the simulation model can guide 3D-printed construct design. In fact, the model is eventually applied to 3D-printed constructs including internal vascularization channels to

show how different geometries can significantly affect cell viability inside the construct.

2. Materials and methods

2.1. Materials

Normal human dermal fibroblasts (HDF) were purchased from Lonza, Basel, Switzerland. Fibroblast culture medium and phosphate-buffered saline (PBS) were purchased from CARLO ERBA Reagents S.r.l., Cornaredo, Italy. Antibiotic/antimycotic solution, gelatin, sodium alginate and calcein AM were purchased from Sigma Aldrich, St. Louis, Missouri, USA. CaCl_2 solution, print cartridges and nozzles were purchased from Twin Helix S.r.l., Rho, Milan.

2.2. Mathematical model of nutrient diffusion and consumption and cell proliferation

In order to represent nutrient diffusion, consumption, and cell proliferation, our newly proposed model consists of three equations: two nonlinear parabolic PDEs describing oxygen and glucose concentrations in a 3D geometry (domain), and an additional unsteady nonlinear PDE describing cell density in every point of the domain. The equations for oxygen and glucose concentrations describe the diffusion and consumption of the two substances. The diffusion term is derived by the combination of the first and the second Fick's laws, which are described in Equations I and II. The diffusion equation is found in Equation III.

$$\vec{J} = -D\vec{\nabla}(\phi) \quad (\text{I})$$

$$\frac{\partial \phi}{\partial t} = -\vec{\nabla} \cdot \vec{J} \quad (\text{II})$$

$$\frac{\partial \phi}{\partial t} - \vec{\nabla} \cdot (D\vec{\nabla}\phi) = 0 \quad (\text{III})$$

The consumption term, describing the rate of nutrient consumed by the cells, is given by the sum of two components: the lag consumption (Equation IV), accounting for the consumption rate for cell survival, and the growth consumption (Equation V), accounting for the consumption rate for cell proliferation. The consumption rate depends not only on the cell density but also on the nutrient concentration. In both the equations, the Michaelis–Menten formulation is used, relating the actual consumption to the maximum consumption rate and the nutrient concentration through the Michaelis–Menten constant. Eventually, the maximum consumption rate is computed as the metabolic consumption of the single cell times the cell density while the Michaelis–Menten constants are the nutrient concentrations at which half of the corresponding maximum consumption rate occurs. In

the growth consumption equation (Equation V), the self-inhibiting effect is introduced through the term $1-\rho/\rho_{\max}$ to account for the reduction of the nutrient consumption rate for cell proliferation when the cell density increases since cell proliferation is limited by the maximum cell density. The diffusion-consumption equation is shown in Equation VI.

$$\psi(\phi, \rho)^{\text{lag}} = V_{\max} \frac{\phi}{\phi + K^m} = m\rho \frac{\phi}{\phi + K^m} \quad (\text{IV})$$

$$\psi(\phi, \rho)^{\text{growth}} = \rho \left(1 - \frac{\rho}{\rho_{\max}} \right) m \frac{\phi}{\phi + K^g} \quad (\text{V})$$

$$\frac{\partial \phi}{\partial t} - \vec{\nabla} \cdot (D\vec{\nabla}\phi) + \psi(\phi) = 0 \quad (\text{VI})$$

The third differential equation of the model describes the pointwise cell proliferation and death and consists of a mass balance equation based on the variation of cell density through specific growth and death rates (Equation VII). The growth rate is described by the Monod equation in a similar way to the Michaelis–Menten equation for nutrient consumption (Equation VIII). To consider at the same time the effect of glucose and oxygen on cellular proliferation, a multiplicative decomposition of the growth rate for the two substances is used. The death rate is introduced as the inverse of the Monod equation (Equation IX). The Monod equation for growth is hybridized with the Lotka–Volterra equation, through the same multiplicative term $(1-\rho/\rho_{\max})$.

$$\frac{\partial \rho}{\partial t} = \rho \left(1 - \frac{\rho}{\rho_{\max}} \right) \mu^g - \rho \mu^d \quad (\text{VII})$$

$$\mu^g = G \left(\frac{\phi}{\phi + K_{O_2}^g} \right) \left(\frac{\phi}{\phi + K_{gl}^g} \right) \quad (\text{VIII})$$

$$\mu^d = -H \left(1 - \frac{\phi}{\phi + K^d} \right) \quad (\text{IX})$$

The diffusion-reaction equations of oxygen and glucose concentration and the mass balance equation for cell density variation are found in Equations X, XI, and XII. To complete the problem, a set of boundary conditions for the diffusion-consumption equations and an initial condition for all three equations are specified. The boundary conditions describe oxygen and glucose concentration at the interface between the culture medium and the construct surface (Equations XIII and XIV). The boundary conditions used are of Robin ones. They can model a wide range of different cases by properly tuning the Robin coefficient, thus allowing for the development of a versatile model. The initial conditions specify the values of oxygen, glucose, and cell concentration in the whole domain at the initial time (Equations XV, XVI, and XVII).

$$\frac{\partial \phi_{O_2}}{\partial t} - \bar{\nabla} \cdot (D_{O_2} \bar{\nabla} \phi_{O_2}) + \psi_{O_2}(\phi_{O_2}, \rho) = 0 \quad \text{in } \Omega, \forall t > 0 \quad (X)$$

$$\frac{\partial \phi_{gl}}{\partial t} - \bar{\nabla} \cdot (D_{gl} \bar{\nabla} \phi_{gl}) + \psi_{gl}(\phi_{gl}, \rho) = 0 \quad \text{in } \Omega, \forall t > 0 \quad (XI)$$

$$\frac{\partial \rho}{\partial t} = \rho \left(1 - \frac{\rho}{\rho_{\max}} \right) G \left(\frac{\phi_{O_2}}{\phi_{O_2} + K_{O_2}^g} \right) \left(\frac{\phi_{gl}}{gl + K_{gl}^g} \right) - \rho H \left(1 - \frac{\phi_{O_2}}{\phi_{O_2} + K^d} \right) \quad (XII)$$

$$-D_{O_2} \bar{\nabla} \phi_{O_2} \cdot \bar{n} = \gamma_{O_2} (\phi_{O_2} - \phi_{O_2}^{OUT}) \quad \text{on } \Gamma, \forall t > 0 \quad (XIII)$$

$$-D_{gl} \bar{\nabla} \phi_{gl} \cdot \bar{n} = \gamma_{gl} (\phi_{gl} - \phi_{gl}^{OUT}) \quad \text{on } \Gamma, \forall t > 0 \quad (XIV)$$

$$\phi_{O_2}(t=0) = \phi_{O_2}^{IN} \quad \text{in } \Omega \quad (XV)$$

$$\phi_{gl}(t=0) = \phi_{gl}^{IN} \quad \text{in } \Omega \quad (XVI)$$

$$\rho(t=0) = \rho^{IN} \quad \text{in } \Omega \quad (XVII)$$

2.2.1. Numerical approximation

The system of equations representing the model (Equations X, XI, XII, XIII, XIV, XV, XVI, and XVII) is solved numerically. For the numerical approximation of the PDEs, the finite element method (FEM) is used. The Galerkin FEM^[22] relies on the reformulation of the strong PDE into its weak formulation and on the construction of a finite-dimensional subspace where the approximate solution is looked for. The spatial 3D domain is discretized with tetrahedra finite elements with piecewise linear basis functions. The PDEs are considered in vectorial form, with the weak formulation of the problem written as the inner product of the vector PDE and the vectorial test function^[23]. Regarding the time domain, a first-order accurate semi-implicit numerical scheme based on backward Euler is implemented, so that the problem is linear in the unknown solution at each time instance. The linear solver used is the Generalized Minimal Residual Method (GMRES) with Incomplete Lower-Upper factorization (ILU) preconditioner. The computation is implemented in FEniCS, an open-source FEM software library. The numerical approximation of the problem is found in Equation XVIII. Time discretization consists in subdividing the time domain into a finite number of time steps. Given T the time length and N the number of time steps, the time step width is given by T/N . Each iteration of the scheme consists of finding the solution at the current time step k , which cycles from 1 to N at each node h of the discretized spatial domain. Equations XIX, XX, and XXI describe the initial conditions of oxygen, glucose, and cell concentration, i.e., at $k = 1$.

$$\begin{aligned} & \int_{\Omega} \left(\frac{\phi_{O_2h}^{(k+1)} - \phi_{O_2h}^{(k)}}{\Delta t} v_{O_2h} + D_{O_2} \bar{\nabla} \phi_{O_2h}^{(k+1)} \cdot \bar{\nabla} v_{O_2h} \right. \\ & \left. + \rho_h^{(k)} m_{O_2}^m \frac{\phi_{O_2h}^{(k+1)}}{\phi_{O_2h}^{(k)} + K_{O_2}^m} + \rho_h^{(k)} \left(1 - \frac{\rho_h^{(k)}}{\rho_{\max}} \right) m_{O_2}^g \frac{\phi_{O_2h}^{(k+1)}}{\phi_{O_2h}^{(k)} + K_{O_2}^g} \right) \partial \Omega \\ & + \int_{\Gamma} \gamma_{O_2} (\phi_{O_2h}^{(k+1)} - \phi_{O_2}^{OUT}) \partial \Gamma + \int_{\Omega} \left(\frac{\phi_{glh}^{(k+1)} - \phi_{glh}^{(k)}}{\Delta t} v_{glh} \right. \\ & \left. + D_{gl} \bar{\nabla} \phi_{glh}^{(k+1)} \cdot \bar{\nabla} v_{glh} + \rho_h^{(k)} m_{gl}^m \frac{\phi_{glh}^{(k+1)}}{\phi_{glh}^{(k)} + K_{gl}^m} \right. \\ & \left. + \rho_h^{(k)} \left(1 - \frac{\rho_h^{(k)}}{\rho_{\max}} \right) m_{gl}^g \frac{\phi_{glh}^{(k+1)}}{\phi_{glh}^{(k)} + K_{gl}^g} \right) \partial \Omega \\ & + \int_{\Gamma} \gamma_{gl} (\phi_{glh}^{(k+1)} - \phi_{gl}^{OUT}) \partial \Gamma + \int_{\Omega} \left(\frac{\rho_h^{(k+1)} - \rho_h^{(k)}}{\Delta t} v_{\rho h} \right. \\ & \left. - \rho_h^{(k+1)} \left(1 - \frac{\rho_h^{(k)}}{\rho_{\max}} \right) G \left(\frac{\phi_{O_2h}^{(k)}}{\phi_{O_2h}^{(k)} + K_{O_2}^g} \right) \left(\frac{\phi_{glh}^{(k)}}{\phi_{glh}^{(k)} + K_{gl}^g} \right) \right. \\ & \left. - \rho_h^{(k+1)} H \left(1 - \frac{\phi_{O_2h}^{(k)}}{\phi_{O_2h}^{(k)} + K^d} \right) \right) \partial \Omega, \text{ for } k = 0, 1, \dots, N_T - 1 \end{aligned} \quad (XVIII)$$

$$\phi_{O_2h}^{(k=0)} = \phi_{O_2}^{IN} \quad \text{in } \Omega \quad (XIX)$$

$$\phi_{glh}^{(k=0)} = \phi_{gl}^{IN} \quad \text{in } \Omega \quad (XX)$$

$$\rho_h^{(k=0)} = \rho^{IN} \quad \text{in } \Omega \quad (XXI)$$

2.2.2. Volume-averaged model

A simplified version of the mathematical model (Equations X, XI, XII, XIII, XIV, XV, XVI, and XVII) was obtained by averaging the PDEs over the spatial domain. Therefore, the point values of oxygen, glucose, and cell concentration are approximated by their volume average over the domain (Equations XXII, XXIII, and XXIV), thus obtaining a system of first-order ordinary differential equations, described in Equations XXV, XXVI, and XXVII. For the time discretization, the semi-implicit discretization scheme based on backward Euler was used (Equations XIX, XX, and XXI). The initial conditions are described in Equations XXVIII, XXIX, and XXX. The numerical model was implemented in Matlab. As in the experiment, 7 days of culture were simulated. The time step was set to 0.001 h. The model parameters are summarized in Table 1.

$$\overline{\phi_{O_2}^{(k)}} = \int_{\Omega} \phi_{O_2}^{(k)} \partial \Omega / |\Omega|, \quad \text{for } k = 0, 1, \dots, N_T - 1 \quad (XXII)$$

$$\overline{\phi_{gl}^{(k)}} = \int_{\Omega} \phi_{gl}^{(k)} \partial \Omega / |\Omega|, \quad \text{for } k = 0, 1, \dots, N_T - 1 \quad (XXIII)$$

$$\overline{\rho^{(k)}} = \int_{\Omega} \rho^{(k)} \partial \Omega / |\Omega|, \quad \text{for } k = 0, 1, \dots, N_T - 1 \quad (XXIV)$$

Table 1. Input parameters of the model to replicate the experimental conditions

Parameter	Value	Ref
D_{O_2}	$10^{-9} [m^2 \cdot s^{-1}]$	[10]
D_{gl}	$10^{-10} [m^2 \cdot s^{-1}]$	[10]
$m_{O_2}^m$	$1.7 \times 10^{-18} [mol \cdot cell^{-1} \cdot s^{-1}]$	[10,24]
m_{gl}^m	$3.5 \times 10^{-17} [mol \cdot cell^{-1} \cdot s^{-1}]$	[10,24]
$m_{O_2}^g$	$2.5 \times 10^{-18} [mol \cdot cell^{-1} \cdot s^{-1}]$	[24]
m_{gl}^g	$1.4 \times 10^{-16} [mol \cdot cell^{-1} \cdot s^{-1}]$	[10]
$\phi_{O_2}^{OUT}$	$0.2 [mol \cdot m^{-3}]$	[10]
ϕ_{gl}^{OUT}	$25 [mol \cdot m^{-3}]$	[10,25]
G	$6.39 \times 10^{-6} [s^{-1}]$	[26]
H	$3.89 \times 10^{-6} [s^{-1}]$	[27]
ρ_{max}	$5 \times 10^{12} [cell \cdot m^{-3}]$	Imposed
$K_{O_2}^m$	$10^{-3} [mol \cdot m^{-3}]$	[24]
K_{gl}^m	$10^{-1} [mol \cdot m^{-3}]$	[28]
$K_{O_2}^g$	$10^{-2} [mol \cdot m^{-3}]$	Imposed
K_{gl}^g	$10^0 [mol \cdot m^{-3}]$	[20]
K_d	$10^{-4} [mol \cdot m^{-3}]$	[29]
$\phi_{O_2}^{in}$	$0 [mol \cdot m^{-3}]$	Imposed
ϕ_{gl}^{in}	$0 [mol \cdot m^{-3}]$	Imposed
ρ_{in}	$1.89414 \times 10^{11} [cell \cdot m^{-3}]$	Imposed
Radius	0.0035	Imposed
Height	0.0005	Imposed

$$\begin{aligned} & \frac{\overline{\phi_{O_2}^{(k+1)}}|\Omega| - \overline{\phi_{O_2}^{(k)}}|\Omega|}{\Delta t} + \gamma_{O_2} \left(\overline{\phi_{O_2}^{(k)}}|\Gamma| - \phi_{O_2}^{OUT}|\Gamma| \right) \\ & + \overline{\rho^{(k)}}|\Omega| \frac{\overline{\phi_{O_2}^{(k+1)}}}{\overline{\phi_{O_2}^{(k)}} + K_{O_2}^m} \\ & + \overline{\rho^{(k)}}|\Omega| \frac{\overline{\phi_{O_2}^{(k+1)}}}{\overline{\phi_{O_2}^{(k)}} + K_{O_2}^g} \left(1 - \frac{\overline{\rho^{(k)}}}{\rho_{max}} \right) = 0 \quad \text{for } k = 0, 1, \dots, N_T - 1 \end{aligned} \quad (XXV)$$

$$\begin{aligned} & \frac{\overline{\phi_{gl}^{(k+1)}}|\Omega| - \overline{\phi_{gl}^{(k)}}|\Omega|}{\Delta t} + \gamma_{gl} \left(\overline{\phi_{gl}^{(k)}}|\Gamma| - \phi_{gl}^{OUT}|\Gamma| \right) \\ & + \overline{\rho^{(k)}}|\Omega| \frac{\overline{\phi_{gl}^{(k+1)}}}{\overline{\phi_{gl}^{(k)}} + K_{gl}^m} + \overline{\rho^{(k)}}|\Omega| \frac{\overline{\phi_{gl}^{(k+1)}}}{\overline{\phi_{gl}^{(k)}} + K_{gl}^g} \left(1 - \frac{\overline{\rho^{(k)}}}{\rho_{max}} \right) = 0, \\ & \text{for } k = 0, 1, \dots, N_T - 1 \end{aligned} \quad (XXVI)$$

$$\frac{\overline{\rho^{(k+1)}}|\Omega| - \overline{\rho^{(k)}}|\Omega|}{\Delta t} - \overline{\rho^{(k)}}|\Omega| \left(1 - \frac{\overline{\rho^{(k)}}}{\rho_{max}} \right)$$

$$\begin{aligned} & G \left(\frac{\overline{\phi_{O_2}^{(k)}}}{\overline{\phi_{O_2}^{(k)}} + K_{O_2}^g} \right) \left(\frac{\overline{\phi_{gl}^{(k)}}}{\overline{\phi_{gl}^{(k)}} + K_{gl}^g} \right) \\ & + \overline{\rho^{(k)}}|\Omega| H \left(1 - \frac{\overline{\phi_{O_2}^{(k)}}}{\overline{\phi_{O_2}^{(k)}} + K_d} \right) = 0, \\ & \text{for } k = 0, 1, \dots, N_T - 1 \end{aligned} \quad (XXVII)$$

$$\overline{\phi_{O_2}^{(k=0)}} = 0 \quad (XXVIII)$$

$$\overline{\phi_{gl}^{(k=0)}} = 0 \quad (XXIX)$$

$$\overline{\rho^{(k=0)}} = 1.89 \cdot 10^{11} [cell \cdot m^{-3}] \quad (XXX)$$

2.3. Experimental validation

The model validation was performed to assess its prediction capability in terms of cell concentration in the 3D geometric model representing the construct. The validation was performed through an experimental campaign of extrusion bioprinting, by assessing cell viability as the number of vital cells within the bioprinted samples over time. The experimental conditions were replicated in the model through the input parameters. For the validation phase, the model was simplified by integrating the variables at each time step over the spatial domain. The outcomes of model and experiment were compared by computing the mean square error between the model prediction and the average value of cell concentration observed in the experiments. An optimization step was first carried out to identify optimal values of the model parameters that minimize the mean square error between experimental and model data. Finally, a sensitivity analysis was performed on these set of parameters that were optimized, to identify the most relevant ones, i.e., the ones that mostly affect the prediction capability of the simulation model.

2.3.1. Extrusion bioprinting

HDF were cultured in fibroblast culture medium with 1% antibiotic/antimycotic solution. Cells were harvested at about 80% confluence. An alginate/gelatin 4%/4% (w/v) bioink was prepared by adding 4 g of gelatin and 4 g of sodium alginate to 100 mL of PBS and leaving the ink on the magnetic stirrer overnight. To ensure sterility of the ink, powders were exposed to ultraviolet light for one hour prior to PBS addition. The bioink was embedded with HDF at a nominal cell concentration of 2×10^6 cells/mL, corresponding to 2×10^{12} cells/m³. The specimens were printed through the BioX bioprinter by selecting the protocol “droplet bioprinting” and by setting the following printing parameters: temperature 30°C, pressure 0.8 kPa, and extrusion time 0.8 second. The bioink was extruded

through a 22G nozzle. After bioprinting, the samples were crosslinked by adding CaCl_2 solution for 3 min, and then rinsed with PBS and immersed in culture medium. The samples were cultured in the incubator at 37°C and 5% CO_2 .

2.3.2. Viability analysis

The analysis of cell viability was performed through fluorescence staining and imaging. The bioprinted specimens were incubated with 500 μL of calcein AM solution, with a calcein concentration of 5 μL in 6 mL PBS and 6 mL HDF culture medium. After one hour of incubation, fluorescence images were taken through a fluorescence microscope (Celena S) in the green channel. Images were taken in the center of each specimen. The Z-stack system was used to take 7 images with a Z step of 30 μm for a total Z span of 180 μm . The area of each image is equal to the field of view of the microscope, i.e., $1.84 \times 1.48 \text{ mm}$. An in-house Matlab code was developed to compute the number of cells in each image. The cell concentration was computed as the cell number divided by the volume inspected, i.e., the field of view multiplied by the thickness of the single layer ($1.84 \times 1.48 \times 0.03 \text{ mm}^3$). The cell concentration was averaged along the seven layers of the z-stack to obtain the mean concentration of each sample. Cell viability in the samples was analyzed at days 1, 2, 3, 4, and 7. At each time step, three samples were analyzed.

2.3.3. Representing the experimental conditions in the volume-averaged model: Input model parameters from the literature

The experimental conditions were replicated in the differential model through the physical and geometrical parameters, which are summarized in Table 1. The diffusivity coefficients for oxygen and glucose in alginate and gelatin hydrogel were taken from McMurtrey^[10]. Diffusivity coefficient of glucose was set to be one order of magnitude smaller than diffusivity coefficient of oxygen, due to the higher dimension of the glucose molecule. The coefficient of metabolic consumption rate of oxygen and glucose by fibroblasts, $m_{\text{O}_2}^m$ and m_{gl}^m , respectively, were taken from Wagner *et al.*^[24]. Growth consumption rates, on the other hand, were not found specifically for fibroblasts, and they were set to the value used by McMurtrey^[10] for mesenchymal stem cells (MSCs). The value of oxygen and glucose concentrations outside the boundary of the bioprinted samples was assumed as the concentrations within the culture medium. The culture medium used was purchased from CARLO ERBA Reagents, and it consists of a basal medium embedded with supplements specific for fibroblasts. Oxygen concentration was taken from McMurtrey^[10]. Glucose concentration was taken from the

Table 2. Models of bioprinted constructs and their dimensions

Construct model	Diameter (mm)	Height (mm)	Channel diameter (mm)
1X	1.5	0.5	Not present
2X	3	1	Not present
3X	4.5	1.5	Not present
3X with channels	4.5	1.5	0.4

data sheet of the culture medium. Since no information was available for the specific culture medium, the parameter was set according to Dulbecco's Modified Eagle Medium (DMEM)^[25], which is a basic medium commonly used for culturing several cell types. The proliferation rate G was calculated based on the exponential cell growth phenomenon, considering a duplication time of 30 h, as stated by Gupta *et al.*^[26]. The death rate H was set in order to observe a decrease in cell viability of 90% after 7 days in a hypoxic environment. It was computed similarly as described elsewhere^[27]. The maximum cell concentration was imposed by considering that a high percentage of the volume of the bioprinted construct should be occupied by cells after proliferation, but fibroblasts occupy a large area when they are attached to the substrate. The maximum cell concentration was set to $5 \times 10^{12} \text{ cells/m}^3$. The Michaelis–Menten and Monod constants were taken from the literature or imposed to a reasonable value to make the computations work. The initial values of oxygen and glucose concentration were set to zero to account for the usage of gas and nutrients by cells during the printing. The initial cell concentration was set to $1.89414 \times 10^{11} \text{ cells/m}^3$, as measured experimentally. Finally, the bioprinted sample was modeled as a cylinder (the computational domain) with diameter 3.5 mm and height 0.5 mm. The diameter of the printed samples was measured through ImageJ. The mean value was 3.6 mm with a range from 2.42 mm and 6.04 mm. The height of the samples was not measured directly, but it was observed by exploring the vertical direction through the fluorescence microscope when taking images, and it was set to 0.5 mm.

2.4. Application of the PDE-based model to bioprinted constructs

The model was exploited to study oxygen and glucose distribution and cell proliferation and death within bioprinted constructs. Constructs of three different dimensions, whose diameter is included in a range of 1.5–4.5 mm, were modeled as summarized in Table 2. Moreover, a model of bioprinted construct with inner channels was implemented, as shown in Figure 1. Bioprinted constructs were modeled to be made of alginate embedded with hMSCs, with an initial concentration of

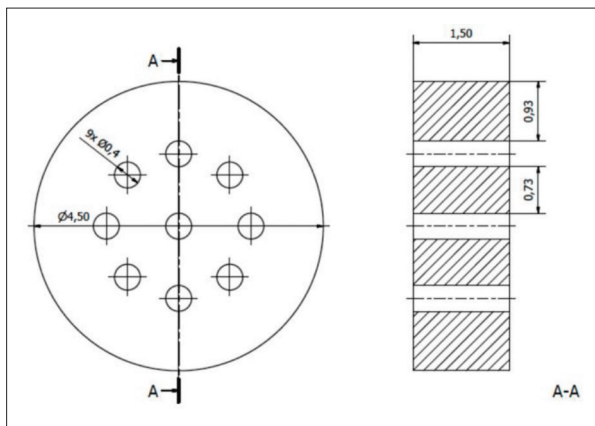


Figure 1. 3X construct modified with nine channels with each having a diameter of 0.4 mm.

Table 3. Input parameters of the model to simulate the bioprinting applicationa

Parameter	Value	Ref
D_{O_2}	$10^{-9} \text{ [m}^2 \cdot \text{s}^{-1}\text{]}$	[10]
D_{gl}	$10^{-10} \text{ [m}^2 \cdot \text{s}^{-1}\text{]}$	[10]
$m_{O_2}^m$	$2 \times 10^{-17} \text{ [mol} \cdot \text{cell}^{-1} \cdot \text{s}^{-1}\text{]}$	[10]
m_{gl}^m	$3.5 \times 10^{-17} \text{ [mol} \cdot \text{cell}^{-1} \cdot \text{s}^{-1}\text{]}$	[10]
$m_{O_2}^g$	$3.8 \times 10^{-17} \text{ [mol} \cdot \text{cell}^{-1} \cdot \text{s}^{-1}\text{]}$	[10]
m_{gl}^g	$1.4 \times 10^{-16} \text{ [mol} \cdot \text{cell}^{-1} \cdot \text{s}^{-1}\text{]}$	[10]
$\phi_{O_2}^{OUT}$	$0.2 \text{ [mol} \cdot \text{m}^{-3}\text{]}$	[10]
ϕ_{gl}^{OUT}	$25 \text{ [mol} \cdot \text{m}^{-3}\text{]}$	[10]
G	$6.94 \times 10^{-6} \text{ [s}^{-1}\text{]}$	[20]
H	$1.9 \times 10^{-6} \text{ [s}^{-1}\text{]}$	[27]
ρ_{max}	$8.8 \times 10^{13} \text{ [cell} \cdot \text{m}^{-3}\text{]}$	Imposed
$K_{O_2}^m$	$10^{-3} \text{ [mol} \cdot \text{m}^{-3}\text{]}$	[24]
K_{gl}^m	$10^{-1} \text{ [mol} \cdot \text{m}^{-3}\text{]}$	[28]
$K_{O_2}^g$	$10^{-2} \text{ [mol} \cdot \text{m}^{-3}\text{]}$	Imposed
K_{gl}^g	$10^0 \text{ [mol} \cdot \text{m}^{-3}\text{]}$	[20]
K_d	$10^{-4} \text{ [mol} \cdot \text{m}^{-3}\text{]}$	[29]
$\phi_{O_2}^{in}$	$0 \text{ [mol} \cdot \text{m}^{-3}\text{]}$	Imposed
ϕ_{gl}^{in}	$0 \text{ [mol} \cdot \text{m}^{-3}\text{]}$	Imposed
ρ_{in}	$11 \times 10^{12} \text{ [cell} \cdot \text{m}^{-3}\text{]}$	[30]

$1.1 \times 10^{13} \text{ cells/m}^3$, as suggested by bioprinting protocols^[30]. The input parameters are summarized in Table 3. The diffusivity coefficients for oxygen and glucose in alginate hydrogel and the oxygen and glucose consumption rates by MSCs were taken from McMurtrey^[10]. Boundary conditions of oxygen and glucose are set according to their oxygen and glucose concentrations found in the culture medium in which the bioprinted constructs are immersed after being printed. The culture medium consists of a basal medium embedded with supplements

specific for fibroblasts. Oxygen concentration was taken from McMurtrey^[10]. Glucose concentration was taken from the data sheet of DMEM, a basic culture medium commonly used for several cell types, according to the product catalog^[25]. The proliferation rate G was calculated based on the exponential cell growth phenomenon, considering a duplication time of 24 h. A similar approach was used by Higuera *et al.*^[20]. The death rate H was set in order to observe a decrease in cell viability of 90% after 14 days in a hypoxic environment, as considered by Niu *et al.*^[27]. The maximum cell concentration was imposed by considering that a high percentage of the volume of the bioprinted construct should be occupied by cells after proliferation. The Michaelis–Menten and Monod constants were taken from the literature. The initial values of oxygen and glucose concentration were set to zero to account for the usage of gas and nutrients by cells during the printing. The initial condition for cell density is given by the initial concentration of cells inserted into the bioink. Initial conditions of oxygen and glucose are set to zero, by assuming that cells would consume the available nutrients during the printing phase, while embedded in the bioink. The simulations account for 8 days of culture of the extrusion-bioprinted constructs immersed in fresh culture medium.

2.5. Statistical analysis

Raw data of cell concentration resulting from the experimental tests were analyzed in Microsoft Excel. For each bioprinted sample, the cell concentration was obtained by computing the average of the cell concentration values over the 7 layers along the Z direction. For each time point, the average cell concentration was obtained by computing the average of the three samples.

3. Results

3.1. Experimental validation

In the following sections, the results of the bioprinting experiment and volume-averaged model validation are described. Cell concentration over time within the bioprinted samples was investigated, and the results are shown in Figure 4A. Each point represents the average cell concentration of three samples. At day 1, cell concentration amounted to $1.89414 \times 10^{11} \text{ cells/m}^3$. Cell concentration increased rapidly up to day 4, when it reached a value of $2.311809 \times 10^{12} \text{ cells/m}^3$. At day 7, cell concentration was $2.215761 \times 10^{12} \text{ cells/m}^3$.

3.2. Cell viability from volume-averaged model

An example of bioprinted specimen and cell imaging are shown in Figures 2 and 3. In Figure 4B, the results of the volume-averaged numerical model in terms of cell density as a function of time are shown, when the experimental

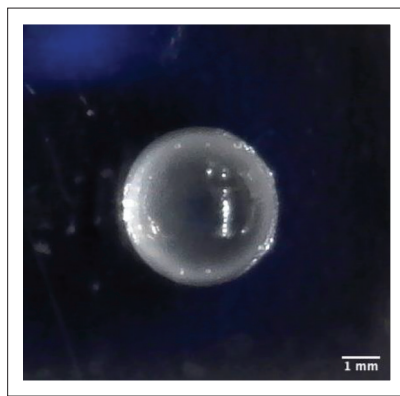


Figure 2. An example of bioprinted sample.

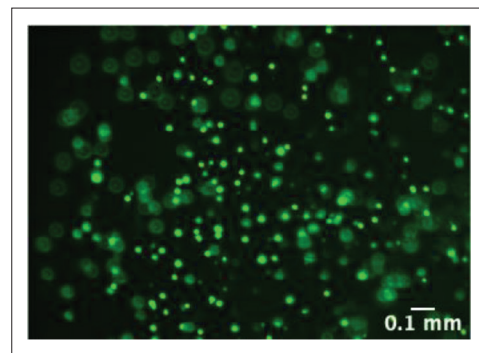


Figure 3. Representative fluorescence microscope image showing the detected cells.

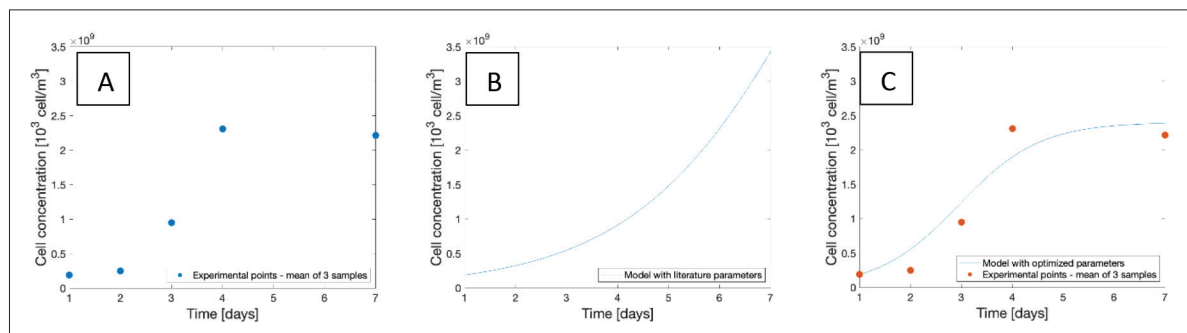


Figure 4. Cell concentration over time. (A) Experimental cell concentration over time at days 1, 2, 3, 4, and 7. Each point represents the average of cell concentrations of three samples, obtained as the average of cell concentration over the seven layers of the Z-stack. (B) Simulated cell density over time resulting from the volume-averaged model by employing parameter values according to experimental conditions and the literature. (C) Simulated cell density over time resulting from the model upon parameter calibration.

conditions of the printing session are modeled, according to Table 1. The plot shows an increasing trend of cell density, which starts from the measured initial value of $1.89414 \times 10^{11} \text{ cells/m}^3$, as in the experimental test, and keeps growing up to day 7. In this section, the result of the parameter calibration of the volume-averaged model is described. The parameter calibration consisted of finding the optimal values of the volume-averaged model parameters that minimize the difference between the experimental and the model outputs. The minimization problem was implemented in Matlab by applying the function *fmincon* to a cost function accounting for the difference between the experimental points and the model curve, which was computed as the normalized mean square error (Equation XXXI)^[23]. The parameters to be optimized were the maximum cell concentration of the bioprinted sample ρ_{\max} , the proliferation rate G , the death rate H , the death parameter K^d and the constants $K_{O_2}^g$ and K_{gl}^g . Figure 4C shows the experimental points of cell density obtained from the printing session and the outcome of the model upon parameter calibration. Cell density obtained from the model is exponentially increasing up to day 4, then it reaches a stable value up to day 7. The original and

optimized values of the parameters are found in Table 4. The value of normalized mean square error (NMSE) with literature parameters is 0.0466, whereas with the optimized parameters, it is 0.0068.

$$NMSE = \frac{1}{n} \frac{\sum (y_{\text{model}} - y_{\text{experiment}})^2}{\sum (y_{\text{experiment}})^2} \quad (\text{XXXI})$$

Upon optimization, a sensitivity analysis of the same parameters was performed by changing one parameter at a time and keeping the others fixed. Each parameter was set to 0.1 and 10 times its original value. Finally, a sensitivity analysis was performed on the dimensions of the bioprinted samples, by exploring the whole range of sample diameters that were obtained experimentally. Table 5 shows the results of the sensitivity analysis in terms of NMSE obtained by varying the parameters one at a time and by setting them to 0.1 and 10 times their original value. Two parameters strongly affect the cell concentration curve: growth rate G and maximum cell density. The highest variation in NMSE is obtained when varying the growth rate G : when G is set to 0.1 times its literature value, the NMSE is 0.1561, whereas when it is set to 10 times its literature value, the

Table 4. Values of the original and optimized input parameters and corresponding normalized mean square error

Parameter	Literature/imposed	Calibrated
G	$6.39 \times 10^{-6} \text{ [s}^{-1}\text{]}$	$2.36 \times 10^{-5} \text{ [s}^{-1}\text{]}$
H	$3.89 \times 10^{-6} \text{ [s}^{-1}\text{]}$	$3.88 \times 10^{-5} \text{ [s}^{-1}\text{]}$
K_d	$10^{-4} \text{ [mol} \cdot \text{m}^{-3}\text{]}$	$8.97 \times 10^{-4} \text{ [mol} \cdot \text{m}^{-3}\text{]}$
ρ_{\max}	$5 \times 10^{12} \text{ [cell} \cdot \text{m}^{-3}\text{]}$	$2.43 \times 10^{12} \text{ [cell} \cdot \text{m}^{-3}\text{]}$
K_{gl}^g	$10^0 \text{ [mol} \cdot \text{m}^{-3}\text{]}$	$8.11 \times 10^0 \text{ [mol} \cdot \text{m}^{-3}\text{]}$
$K_{O_2}^g$	$10^{-2} \text{ [mol} \cdot \text{m}^{-3}\text{]}$	$4.13 \times 10^{-2} \text{ [mol} \cdot \text{m}^{-3}\text{]}$
NMSE	0.0466	0.0068

Abbreviation: NMSE, normalized mean square error.

NMSE rises to 0.8498. The model displays the highest sensitivity to this parameter. The maximum cell density is another parameter which strongly affects the model. By varying its value from 0.1 to 10 times its original value, NMSE changes from 0.1290 to 0.0781. The variation of the Monod constants has some effect on cell concentration, too. The value of NMSE = 0.0068 was also observed to be constant when varying the sample diameter from the minimum observed value of 2.42 mm to the maximum observed value of 6.04 mm.

3.3. PDE-based model of cell viability in bioprinted constructs

In this section, the evolution of oxygen, glucose, and cell concentration within the bioprinted constructs resulting from the numerical simulation of the FEM is described. Plots of Figure 5 show the time trends for the smallest and the largest values in space for the investigated variables, i.e., oxygen, glucose, and cell density, within the four different models of bioprinted constructs, i.e., 1X, 2X, 3X and 3X with channels, as a function of culture time. Categories I and II of Figure 5 show that all three constructs receive the same maximum value of oxygen and glucose concentration, which is reached almost immediately and amounts to 0.2 and 25 mM, respectively. The three constructs also present the same maximum value of cell density (category III of Figure 5), which shows a monotonic increasing pattern that reaches a maximum value of $8 \times 10^{13} \text{ cells/m}^3$. However, higher dimensions of the constructs result in a decrease in the minimum value of oxygen and glucose concentration. As far as glucose is concerned, a slight decrease occurs as the dimension increases. For oxygen, instead, in the 2X construct, the minimum value of oxygen concentration decreases below the $K_{O_2}^g$ constant, i.e., the Michaelis–Menten constant for cell proliferation (category I of Figure 5B). In the 3X construct, oxygen concentration decreases below the $K_{O_2}^m$ constant, i.e., the Michaelis–Menten constant for cell survival (category I of Figure 5C). Cell density pattern is different among the different sizes of

Table 5. Value of NMSE obtained by varying each parameter at once to 0.1 and 10 times its original value. NMSE values obtained upon variation of the parameter value, which is set to 0.1X its literature value (column 2) and to 10X its literature value (column 3), while all the other parameters are set to their literature values

Parameter	Literature value $\times 0.1$	Literature value $\times 10$
G	0.1561 ^a	0.8498 ^a
H	0.0466	0.0468
K_d	0.0466	0.0468
ρ_{\max}	0.1290 ^a	0.0781 ^a
K_{gl}^g	0.0449	0.0743
$K_{O_2}^g$	0.0446	0.0806

^aNMSE values obtained upon variation of the parameter value, corresponding to the parameters that influence the model outcome the most.

the constructs (category III of Figure 5). In particular, the 1X construct shows the same monotonic increase of cell density in time for both the smallest and the largest values of cell density (category III of Figure 5A). The 2X construct shows a monotonic increasing pattern, but the minimum value reaches a peak that is slightly lower than the peak of maximum value (category III of Figure 5B). The largest construct, instead, reaches a much lower peak, and it shows a reduction in cell density over time, which means that cell death has occurred (category III of Figure 5C). The pattern of oxygen and glucose concentration as well as cell density of the 3X construct with internal channels is similar to that of the 2X construct (categories I, II, and III of Figure 5D).

Figure 6 shows the spatial distribution of oxygen, glucose, and cell density in the four models of bioprinted constructs after 8 days of culture. The minimum values of oxygen, glucose, and cell density were reached in the areas of the bioprinted constructs located the furthest from the boundaries, i.e., in the central part of the 1X, 2X, and 3X construct models and in the areas between the outer surface and the inner channels of the model of the construct with channels. Oxygen availability is reduced in the 2X construct, which shows an internal region with lower concentration values (category I of Figure 6B). These values are further reduced in the 3X construct, where the low concentration region constitutes almost the whole construct (category I of Figure 6C). Glucose concentration was kept at a high level and showed a slight decrease as the dimension was increased. Regarding cell density, it was increasingly reduced in the central part of the larger constructs, constituting a proper necrotic core in the central part of the 3X construct model (category III of Figure 6C). However, necrotic areas are avoided when introducing channels within the construct, where only a

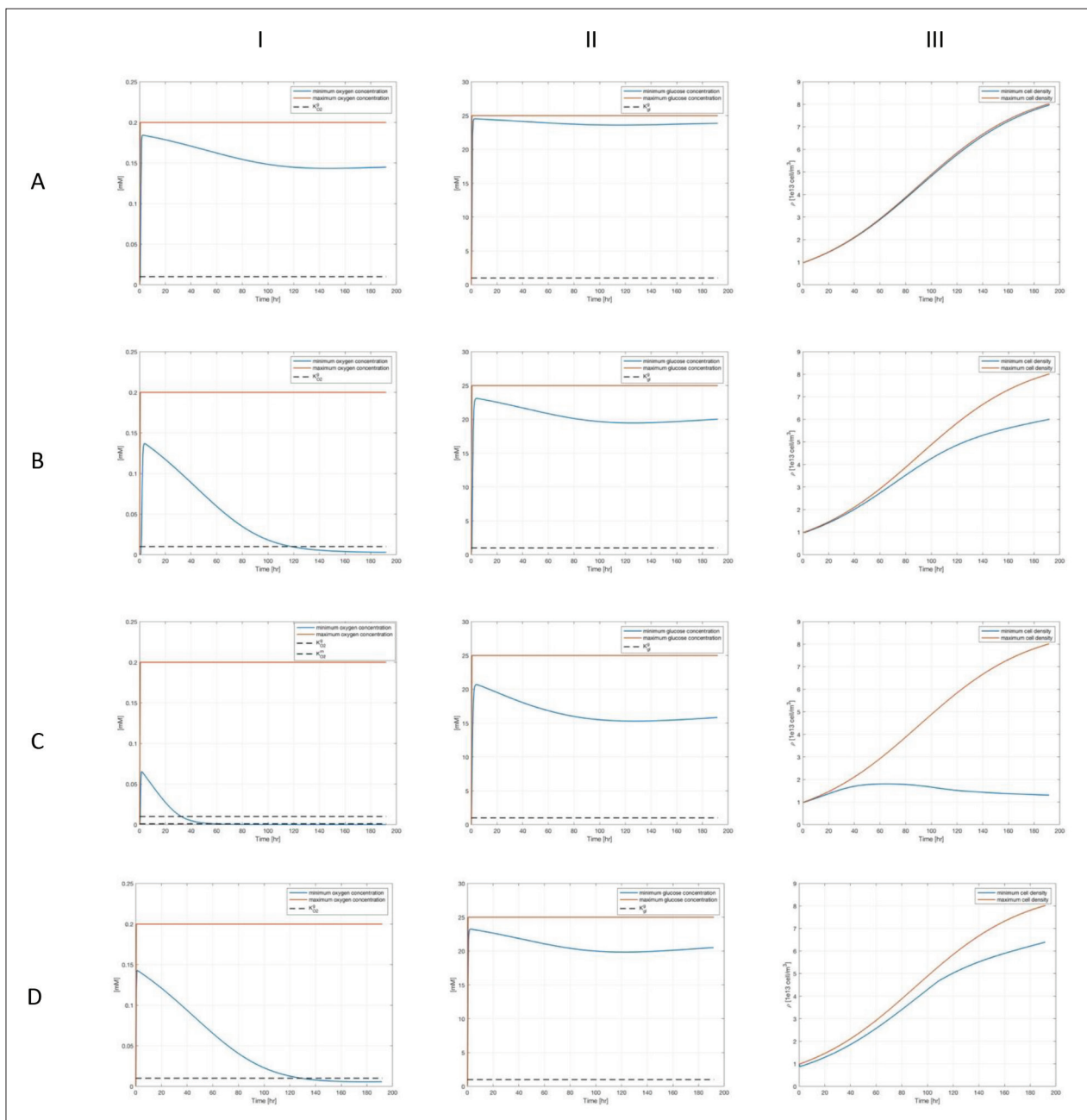


Figure 5. Time evolution of the smallest (blue) and the largest (orange) values of the model variables (I: oxygen; II: glucose; III: cell density) in the domain for four different models of bioprinted specimens (A: 1X; B: 2X; C: 3X; and D: 3X with channels). The dotted lines represent the Monod constants.

slight decrease in cell density in the inner areas occurs even in the largest construct (category III of Figure 6D).

4. Discussion

In this work, a mathematical and computational model of oxygen and glucose diffusion and consumption and cell proliferation and death was developed. The PDE-based model derives from the combination of many aspects

found in the literature and it presents some innovative features with respect to the existing ones. The model accounts for two main nutrients, oxygen and glucose, and their cooperating effect on cell proliferation and death. The consumption phenomenon was described through the Monod equations. Besides, self-promoting and self-inhibiting effects of cells were introduced through the Lotka–Volterra term and the cell density threshold value. The phenomena are analyzed in the whole 3D domain and

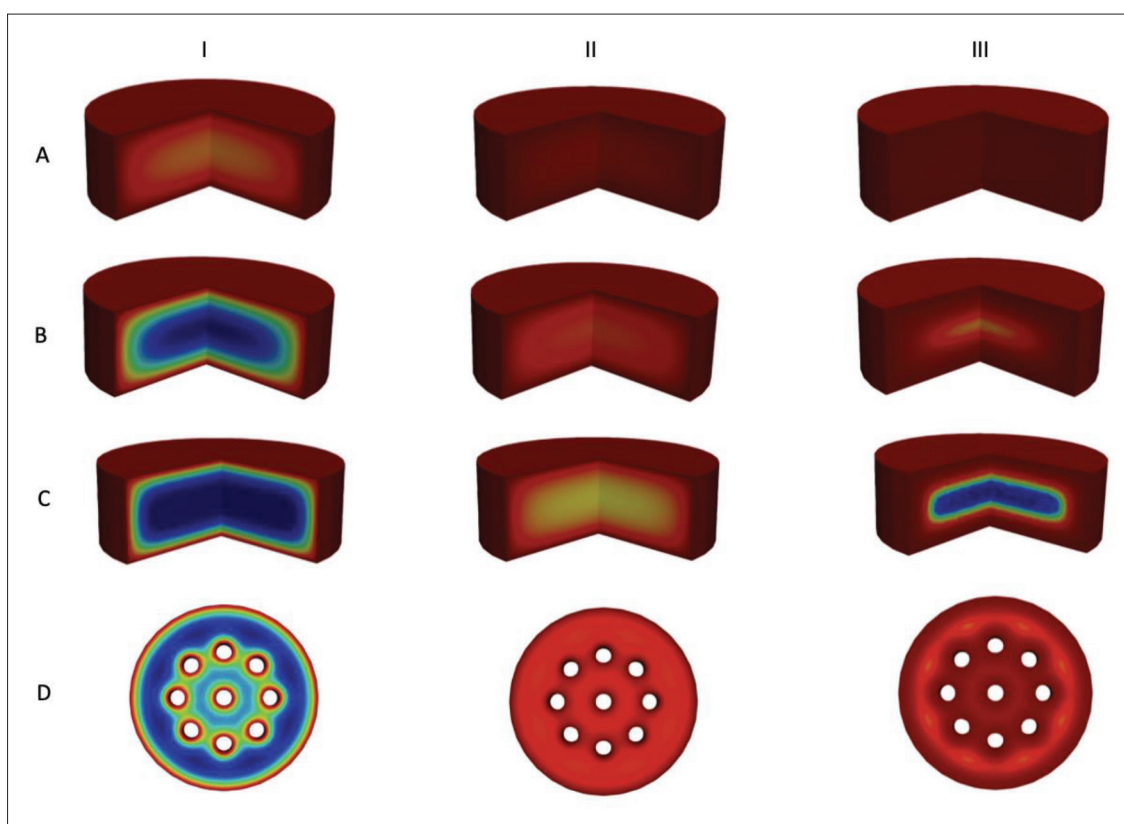


Figure 6. Spatial distribution of the investigated variables (I: oxygen; II: glucose; and III: cell density) within the four different models of bioprinted specimens (A: 1X; B: 2X; C: 3X; and D: 3X with channels).

can be adapted to complex 3D geometries, differently from existing works that already implement these features but are simplified to one preferential direction; for instance, Higuera *et al.*^[20] applied the study to a 2D culture, or Xu *et al.*^[21] developed a realistic model of diffusion and consumption that can be applied to 3D bioprinting, but neglected three-dimensionality of the phenomena and solved it analytically. In the context of 3D bioprinting, which allows for freedom in the design to create complex shapes and is intended to be used for the manufacturing of 3D tissues and organs, it is of great importance to analyze the spatial variations in the whole 3D geometry. The model is intended to be applied to constructs of any material, size, and geometry, as far as the hypothesis of continuum mechanics holds. Once the most appropriate parameter values are set, as supported by the sensitivity analysis, the model can be used to simulate different scenarios and to realize predictions. The computational domain allows for modeling complex geometries, making it suitable to study diverse and multiscale features that are typical of biological tissues obtained through 3D bioprinting. In particular, the introduction of channels is of particular interest, and it can be implemented in the model by changing the geometry of the domain and by

applying the boundary conditions at the interface with the solid construct.

We hereby discuss some limitations of the current model. The cell-embedded hydrogel matrix was modeled as a continuum and the diffusivity coefficient was taken from the literature. Yet, the effects of crosslinking were not included in the model. Experimental studies will be needed to provide a deeper insight into the effects of the crosslinking degree on nutrient diffusivity, which can be implemented easily in the model through the diffusivity coefficient. Possible interactions of nutrients with the proteins of the hydrogel would also need attention and would require additional terms in the equations.

A preliminary validation of the volume-averaged model, yielding a system of ordinary differential equations, was carried out. For this purpose, an experimental test of extrusion bioprinting and viability assessment was carried out. A basic model of 3D constructs was chosen for extrusion bioprinting of cells embedded into a bioink, which resulted in droplet-shaped constructs. This basic geometry allows for easy inspection and analysis yet constitutes a model of bioprinted construct. Although the vertical dimension is small, cells are embedded in a hydrogel matrix; therefore,

the environmental conditions to which cells are subjected in bioprinted samples are modeled, as opposed to the plane 2D cultures. A cell density of 2×10^{12} cells/m³ was selected based on other works found in the literature with similar values^[31]. The bioink of alginate and gelatin was chosen due to the good properties of gelatin since it promotes cell viability and proliferation, combined with alginate to obtain better printability properties. Similar combinations of alginate and gelatin are found in other works^[32,33]. The initial value of cell density of day 1 measured was lower than the nominal one, which was set to 2×10^{12} cells/m³. The causes of such cell loss are not completely clear. It could be partially due to the rate of death during the printing phase, where cells are subjected to high shear stresses. Besides, many intermediate steps take place before the printing stage is reached; therefore, cell loss is plausible. The first days of culture did not result in substantial cell proliferation, which is possibly due to damage to cells of extrusion-based bioprinting or due to a lag time to find attachment sites. A decrease of cell concentration was reported by Sarker *et al.*^[34], who observed this reduction when RGD attachment sites of gelatin are released over the incubation time, pointing out the issue of cell attachment in 3D matrices. Cell density then shows a steep increase up to day 4 and consequent stabilization up to day 7. The model, provided with input parameters corresponding to the experimental conditions, predicts a monotonic increase in cell density over time. The mismatch between the experimental and numerical outcomes consists primarily in the observation of a plateau in the experiment versus a continuous cell growth in the simulation. Since the input parameters taken from the literature do not assume specific values but are found within wide ranges and display uncertainty in their measurement, a parameter optimization step was introduced. In particular, the growth rate, the death rate, and the maximum number of cells turned out to be lower than were assumed. The model does not include the aspects of cell damage and cell attachment, which we believe to be the reason why the horizontal pattern between day 1 and day 2 is not met by the model. Yet, when correctly calibrating the model parameters, a much more similar pattern is found.

Moreover, the parameters affecting the outcome of the model the most were identified through a sensitivity analysis step. The growth rate and the maximum cell density were observed as the most important ones; therefore, they need to be chosen accurately. The growth rate being one of the most important parameters is reasonable since it appears in the mass balance equation and affects the change in cell density directly. The optimized value of the growth rate was found to be half the one found in the literature. This is consistent with the assumption of decreased

metabolism of cells in 3D environments, especially in the first days after bioprinting. The maximum cell density is important because it provides an asymptote to the value that cell density can reach and is therefore linked to the maximum number of cells observed. The maximum cell density after the optimization process was found to be half of the assumed one. In the original setting, cell density increases until the last day of observation, whereas in the optimized setting, the increase of cell density is limited by this parameter. The Monod constants have some limited effects on the outcome of the model. When comparing their values in the original and optimized configurations, they are found within the same ranges. Given these results, the growth rate and the maximum cell density need to be chosen accurately.

The parameters of the model are influenced by many factors. In fact, different cells have a different growth rate, which also depends on the environmental conditions, such as 2D versus 3D culture, bioink formulation, and stiffness of the material. The surface occupied by cells and thus the maximum cell concentration also changes according to cell type. Therefore, when using a numerical model of the type developed in this study, one must invest some effort in defining the proper values of growth rate and maximum cell density. Other printing sessions will follow, in order to explore different conditions and assess the predictive capability of the model.

A further step was made with the simulation of a plausible bioprinting experiment. We were interested in understanding the phenomena of nutrient diffusion and consumption that lead to impaired cell proliferation far from vascular channels. For this reason, small samples in a size range of 1.5–4.5 mm were analyzed. Bioprinted constructs made of alginate embedded with MSCs were modeled. MSCs represent one of the most eligible cell types for bioprinting, since they can be differentiated into other cell types by applying specific stimuli. A future perspective of bioprinting is in fact to regenerate patients' injured tissues by using their own stem cells. Alginate was chosen due to its high versatility and good printing properties. One of the main implications of bioprinting is the possibility to create constructs with high cell density. For this reason, a cell density of 1.1×10^{13} cells/m³ was considered, as also suggested by bioprinting protocols^[30]. Constructs of different sizes were modeled. Different sizes of the constructs resulted in different distributions of nutrients and cells within the constructs. Areas with oxygen concentration lower than $K_{O_2}^g$ are associated with areas where cell density does not increase. Moreover, in areas where oxygen concentration is even lower than $K_{O_2}^m$, cell density starts to decrease abruptly, and cell death occurs, leading to a necrotic region. This proves that oxygen

is the critical substance for cell survival, and it confirms the hypothesis that lack of nutrients in large tissues is likely to occur. To study the effect of vascularization on cell proliferation, internal channels in the largest construct model were introduced. The simulations of bioprinted constructs forecast a spatial gradient of cell density within the construct, and a clear presence of a necrotic core in constructs of 4.5 mm diameter. When vascular channels are introduced, the availability of nutrients is redistributed, leading to a more uniform cell density within the construct. This clearly highlights the importance of introducing vascular networks in bioprinted constructs, especially with large dimensions and high cell concentration. This is aligned with the literature, where many works have attempted creating vascular networks within constructs^[35-37]. A lot of effort is invested in bioprinting toward the fabrication of vascularized tissues, with different strategies being investigated. Direct and indirect extrusion bioprinting are the most common ones. The former consists of the direct fabrication of tissues composed of different cells, including vascular ones. The latter consists of printing a sacrificial ink to be removed afterward to create the channel. Structural stability and resolution remain as the main limitations of these techniques, which are therefore not suitable for the recapitulation of capillary networks. Light-assisted bioprinting, in particular digital light processing, can overcome resolution issues and is used for the fabrication of perfusable constructs, but the types of materials that can be printed are limited and only one material can be printed at a time. The computational model presented here would allow the user to design the specific vascular structure that is needed to keep the tissue of interest viable, thus helping in the selection of the most suitable bioprinting technique^[38].

5. Conclusion

A PDE-based model was developed and simulated at the computer for studying cell proliferation in bioprinted constructs in terms of oxygen and glucose diffusion and consumption as well as cell growth and death rates. The computational model was employed to study oxygen and glucose distribution within bioprinted constructs, and to analyze the entity of the diffusion and consumption phenomena and their effect on cell proliferation and death. The need of vascularization in areas far from the boundaries was confirmed. The model also acts as a tool for designing bioprinted tissues, providing important information on the most penalized regions of the tissue that would need additional care, such as by introducing a vascular network for nutrient supply and waste removal, according to construct geometry, bioink or extracellular matrix properties, and cell activity. Besides, a volume-averaged, ordinary differential equation-based model was

developed, and it was fed with experimental data to compare experimental and computational results. Thus, it constitutes a proof of concept of a digital twin for bioprinting, where the outcome of the bioprinted construct is predicted through the implementation of phenomenological models together with data accounting for the high variability of biological applications. The preliminary validation of the model was performed on simple droplet-shaped constructs. The model was applied to the study of constructs with different sizes and geometries, i.e., with and without channels. More complex configurations of bioprinted constructs, with larger size and hierarchical vascular networks, are going to be investigated both experimentally and computationally, with the aim of fabricating vascularized bioprinted tissues.

Acknowledgments

None.

Funding

This research was partially funded by the European Commission under the “HORIZON-CL4-2021-DIGITAL-EMERGING-01 project BioProS - Biointelligent Production Sensor to Measure Viral Activity” (grant agreement no. 101070120), 2022-2026.”

Conflict of interest

The authors declare no conflict of interests.

Author contributions

Conceptualization: Ludovico Petraro, Patrizia Gironi, Silvia Santoni, Luca Dedè, Bianca Maria Colosimo

Data curation: Ludovico Petraro, Patrizia Gironi

Formal analysis: Ludovico Petraro, Patrizia Gironi, Silvia Santoni

Funding acquisition: Bianca Maria Colosimo, Luca Dedè

Investigation: Ludovico Petraro, Patrizia Gironi

Methodology: Ludovico Petraro, Patrizia Gironi, Silvia Santoni

Project administration: Bianca Maria Colosimo, Luca Dedè, Patrizia Gironi

Resources: Bianca Maria Colosimo, Luca Dedè

Software: Ludovico Petraro, Patrizia Gironi

Supervision: Luca Dedè, Bianca Maria Colosimo

Visualization: Patrizia Gironi, Silvia Santoni

Writing—original draft: Ludovico Petraro, Patrizia Gironi

Writing—review & editing: Patrizia Gironi, Silvia Santoni, Luca Dedè, Bianca Maria Colosimo

Ethics approval and consent to participate

Not applicable. The primary cells (CC-2511) were purchased from Lonza, Basel, Switzerland.

Consent for publication

Not applicable.

Availability of data

Not applicable.

Further disclosure

Part of this work was delivered as an oral presentation at the fifth International Conference on Biomaterials and Nanomaterials, March 10, 2022, Microsoft Teams.

References

- Ng WL, Chua CK, Shen YF, 2019, Print me an organ! Why we are not there yet. *Progr Polym Sci*, 97: 101–145.
<https://doi.org/10.1016/j.progpolymsci.2019.101145>
- Dey M, Ozbolat IT, 2020, 3D bioprinting of cells, tissues and organs. *Sci Rep*, 10(1): 14023.
<https://doi.org/10.1038/s41598-020-70086-y>
- Santoni S, Gugliandolo SG, Sponchioni M, *et al.*, 2022, 3D bioprinting: Current status and trends—A guide to the literature and industrial practice. *Bio-Des Manuf*, 5(1): 14–42.
<https://doi.org/10.1007/s42242-021-00165-0>
- Alexander AE, Wake N, Chepelev L, *et al.*, 2021, A guideline for 3D printing terminology in biomedical research utilizing ISO/ASTM standards. *3D Print Med*, 7(1): 8.
<https://doi.org/10.1186/s41205-021-00098-5>
- Moroni L, Boland T, Burdock JA, *et al.*, 2018, Biofabrication: A guide to technology and terminology. *Trends Biotechnol*, 36(4): 384–402.
<https://doi.org/10.1016/j.tibtech.2017.10.015>
- Ozbolat IT, Hospodiuk M, 2016, Current advances and future perspectives in extrusion-based bioprinting. *Biomaterials*, 76: 321–343.
<https://doi.org/10.1016/j.biomaterials.2015.10.076>
- Ng WL, Huang X, Shkolnikov V, *et al.*, 2022, Controlling droplet impact velocity and droplet volume: Key factors to achieving high cell viability in sub-nanoliter droplet-based bioprinting. *Int J Bioprint*, 8(1): 1–17.
<https://doi.org/10.18063/IJB.V8I1.424>
- Long WL, Lee JM, Zhou M *et al.*, 2020, Vat polymerization-based bioprinting—Process, materials, applications and regulatory challenges. *Biofabrication*, 12(2): 022001.
<https://doi.org/10.1088/1758-5090/ab6034>
- Piazza DE, Pandolfi E, Cacciotti I, *et al.*, 2021, Bioprinting technology in skin, heart, pancreas and cartilage tissues: Progress and challenges in clinical practice. *Int J Environ Res Public Health*, 18(20): 10806.
<https://doi.org/10.3390/ijerph182010806>
- Zhu W, Qu X, Zhu J, *et al.*, 2016, Analytic models of oxygen and nutrient diffusion, metabolism dynamics, and architecture optimization in three-dimensional tissue constructs with applications and insights in cerebral organoids. *Tissue Eng Part C Methods*, 22(3): 221–249.
<https://doi.org/10.1089/ten.TEC.2015.0375>
- Zhu W, Qu X, Zhu J, *et al.*, 2017, Direct 3D bioprinting of prevascularized tissue constructs with complex microarchitecture. *Biomaterials*, 124: 106–115.
<https://doi.org/10.1016/j.biomaterials.2017.01.042>
- Ehsan SM, George SC, 2013, Nonsteady state oxygen transport in engineered tissue: Implications for design. *Tissue Eng Part A*, 19(11–12): 1433–1442.
<https://doi.org/10.1089/ten.tea.2012.0587>
- Magliaro C, Mattei G, Iacoangeli F, *et al.*, 2019, Oxygen consumption characteristics in 3D constructs depend on cell density. *Front Bioeng Biotechnol*, 7: 251.
<https://doi.org/10.3389/fbioe.2019.00251>
- Jin H, Lei J, 2014, A mathematical model of cell population dynamics with autophagy response to starvation. *Math Biosci*, 258: 1–10.
<https://doi.org/10.1016/j.mbs.2014.08.014>
- Vogels M, Zoeckler R, Stasiw DM, *et al.*, 1975, P.F. Verhulst's 'Notice sur la loi que la populations suit dans son accroissement' from Correspondence Mathematique. *Ghent*, X:1838. *J Biol Phys* 3: 183–192.
<https://doi.org/10.1007/BF02309004>
- Ward JP, King JR, 1997, Mathematical modelling of avascular-tumour growth. [Online].
<https://academic.oup.com/imammb/article/14/1/39/660000>
- Kiran KL, Jayachandran D, Lakshminarayanan S, 2009, Mathematical modelling of avascular tumour growth based on diffusion of nutrients and its validation. *Can J Chem Eng*, 87(5): 732–740.
<https://doi.org/10.1002/cjce.20204>
- Tindall MJ, Please CP, Peddie MJ, 2008, Modelling the formation of necrotic regions in avascular tumours. *Math Biosci*, 211(1): 34–55.
<https://doi.org/10.1016/j.mbs.2007.09.002>
- Fritz M, Lima EABF, Nikolić V, *et al.*, 2019, Local and nonlocal phase-field models of tumor growth and invasion due to ECM degradation. *Math Models Methods Appl Sci*, 29(13): 2433–2468.
<https://doi.org/10.1142/S0218202519500519>

20. Higuera G, Schop D, Janssen F, *et al.*, Quantifying in vitro growth and metabolism kinetics of human mesenchymal stem cells using a mathematical model. [Online]. www.liebertpub.com
21. Xu P, 2020, Analytical solution for a hybrid Logistic-Monod cell growth model in batch and continuous stirred tank reactor culture. *Biotechnol Bioeng*, 117(3): 873–878.
<https://doi.org/10.1002/bit.27230>
22. Quarteroni A, 2017, Numerical Models for Differential Problems, MS&A-Modeling, Simulation and Applications 16. [Online]. Accessed: December 06, 2022. <https://link.springer.com/book/10.1007/978-3-319-49316-9>
23. Petter Langtangen H, Logg A, 2017, Solving PDEs in Python—The FEniCS tutorial volume I.
24. Wagner BA, Venkataraman S, Buettner GR, 2011, The rate of oxygen utilization by cells. *Free Radic Biol Med*, 51(3): 700–712.
<https://doi.org/10.1016/j.freeradbiomed.2011.05.024>
25. ThermoFisher Scientific. DMEM - Dulbecco's Modified Eagle Medium. Available on-line. <https://www.thermofisher.com/order/catalog/product/11965092?SID=srch-srp-11965092>.
26. Gupta SC, Gupta N, Ahlawat SPS, *et al.*, 2005, In vitro culture of skin fibroblast cells for potential cloning by nuclear transfer, in *Applications of Gene-Based Technologies for Improving Animal Production and Health in Developing Countries*, Berlin/Heidelberg, Springer-Verlag, 631–640.
https://doi.org/10.1007/1-4020-3312-5_47
27. Niu H, Li C, Guan Y, *et al.*, 2020, High oxygen preservation hydrogels to augment cell survival under hypoxic condition. *Acta Biomater*, 105: 56–67.
<https://doi.org/10.1016/j.actbio.2020.01.017>
28. Gruetter R, Ugurbil K, Seaquist ER, 1998, Steady-state cerebral glucose concentrations and transport in the human brain. *J Neurochem*, 70(1): 397–408.
<https://doi.org/10.1046/j.1471-4159.1998.70010397.x>
29. Buchwald P, 2009, FEM-based oxygen consumption and cell viability models for avascular pancreatic islets. *Theor Biol Med Model*, 6(1): 5.
<https://doi.org/10.1186/1742-4682-6-5>
30. CELLINK Series. [Online]. www.cellink.com
31. Dai LG, Dai NT, Chen TY, *et al.*, 2022, A bioprinted vascularized skin substitute with fibroblasts, keratinocytes, and endothelial progenitor cells for skin wound healing. *Bioprinting*, 28: e00237
<https://doi.org/10.1016/j.bprint.2022.e00237>
32. Krishnamoorthy S, Zhang Z, Xu C, 2019, Biofabrication of three-dimensional cellular structures based on gelatin methacrylate–alginate interpenetrating network hydrogel. *J Biomater Appl*, 33(8): 1105–1117.
<https://doi.org/10.1177/0885328218823329>
33. Yao B, Hu T, Cui X, *et al.*, 2019, Enzymatically degradable alginate/gelatin bioink promotes cellular behavior and degradation in vitro and in vivo. *Biofabrication*, 11(4): 045020.
<https://doi.org/10.1088/1758-5090/ab38ef>
34. Sarker B, Singh R, Zehnder T, *et al.*, 2017, Macromolecular interactions in alginate-gelatin hydrogels regulate the behavior of human fibroblasts. *J Bioact Compat Polym*, 32(3): 309–324.
<https://doi.org/10.1177/0883911516668667>
35. Zhang Y, Kumar P, LvS, *et al.*, 2021, Recent advances in 3D bioprinting of vascularized tissues. *Mater Des*, 199: 109398.
<https://doi.org/10.1016/j.matdes.2020.109398>
36. Novosel EC, Kleinbans C, Kluger PJ, 2011, Vascularization is the key challenge in tissue engineering. *Adv Drug Deliv Rev*, 63(4): 300–311.
<https://doi.org/10.1016/j.addr.2011.03.004>
37. Li X, Liu L, Zhang X, *et al.*, 2018, Research and development of 3D printed vasculature constructs. *Biofabrication*, 10(3).
<https://doi.org/10.1088/1758-5090/aabd56>
38. Zhu J, Wang Y, Zhong L, *et al.*, 2021, Advances in tissue engineering of vasculature through three-dimensional bioprinting. *Dev Dynamics*, 250(12): 1717–1738.
<https://doi.org/10.1002/dvdy.385>